Cancer Research

Myc Expression Drives Aberrant Lipid Metabolism in Lung Cancer

Zoe Hall[1,2], Zsuzsanna Ament[1,2], Catherine H. Wilson[1], Deborah L. Burkhart[1], Tom Ashmore[1], Albert Koulman[2], Trevor Littlewood[1], Gerard I. Evan[1], and Julian L. Griffin[1,2]

Abstract

MYC-mediated pathogenesis in lung cancer continues to attract interest for new therapeutic strategies. In this study, we describe a transgenic mouse model of KRAS-driven lung adenocarcinoma that affords reversible activation of MYC, used here as a tool for lipidomic profiling of MYC-dependent lung tumors formed in this model. Advanced mass spectrometric imaging and surface analysis techniques were used to characterize the spatial and temporal changes in lipid composition in lung tissue. We found that normal lung tissue was characterized predominantly by saturated phosphatidylcholines and phosphatidylglycerols, which are major lipid components of pulmonary surfactant. In contrast, tumor tissues displayed an increase in phosphatidylinositols and arachidonate-containing phospholipids that can serve as signaling precursors. Deactivating MYC resulted in a rapid and dramatic decrease in arachidonic acid and its eicosanoid metabolites. In tumors with high levels of MYC, we found an increase in cytosolic phospholipase A2 (cPLA2) activity with a preferential release of membrane-bound arachidonic acid, stimulating the lipoxygenase (LOX) and COX pathways also amplified by MYC at the level of gene expression. Deactivating MYC lowered cPLA2 activity along with COX2 and 5-LOX mRNA levels. Notably, inhibiting the COX/5-LOX pathways *in vivo* reduced tumor burden in a manner associated with reduced cell proliferation. Taken together, our results show how MYC drives the production of specific eicosanoids critical for lung cancer cell survival and proliferation, with possible implications for the use of COX and LOX pathway inhibitors for lung cancer therapy. *Cancer Res; 76(16); 4608–18. ©2016 AACR.*

Introduction

Non–small cell lung cancer is a leading cause of cancer-related death. The single name encompasses several genetically distinct pathologies, and increasingly efforts to identify therapies for this disease have attempted to target specific mutations. In adenocarcinoma, more than a third of tumors have an activating mutation in KRAS, and MYC has been shown to be frequently overexpressed (1). Although the oncogenic activation of MYC results in uncontrolled cell proliferation (2), MYC inhibition leads to tumor regression and redifferentiation of cells (3, 4). As such MYC is an attractive candidate for cancer drug therapies; however, all its functions and interactions are not fully understood.

Cancer cell proliferation is typically accompanied by metabolic reprogramming, with increased glucose uptake and aerobic glycolysis, as part of the Warburg effect (5). In addition, cancer cells synthesize lipids through *de novo* lipogenesis (5). These lipids play a structural role in new cell membranes and are likely to be further involved in signaling events important for cancer development (5, 6). Although the precise role of aberrant lipid biosynthesis is unknown, several studies have shown that the lipid profile has been linked to survival, ER status, and tumor grade in human breast cancer (7, 8). The lipid composition of tumors is also affected by dynamic processes, having been observed to vary with cell proliferation, apoptosis, and necrosis (9). Furthermore, a recent study has revealed distinct lipid signatures in MYC- or RAS-induced lymphoma, suggesting that the observable lipid profile can be related to specific oncogene expression (10). In addition to genotype specificity, evidence suggests that metabolic profiles are highly tissue specific (11).

Here, we use a novel transgenic mouse model of $KRAS^{G12D}$-driven lung adenocarcinoma with reversible activation of MYC, to study changes to the lung lipid profile following tumorigenesis with high MYC activity, and subsequent deactivation of MYC over time. We characterized the changes in lipid composition and abundance using matrix-assisted laser desorption ionization-mass spectrometry imaging (MALDI-MSI) and liquid extraction surface analysis-mass spectrometry (LESA-MS). MALDI-MSI is ideally placed for *in situ* molecular mapping since lipids are directly ablated and ionized from tissue by a moving laser pulse, retaining critical spatial information (12–15). In LESA-MS lipids are extracted directly from the surface of tissue with solvent, providing an orthogonal approach to the direct analysis of lipids from tissues (16–18). This allowed us to follow lipidome changes and to map these effects across the tissue.

[1]Department of Biochemistry, University of Cambridge, Cambridge, United Kingdom. [2]MRC Human Nutrition Research, Cambridge, United Kingdom.

Note: Supplementary data for this article are available at Cancer Research Online (http://cancerres.aacrjournals.org/).

Z. Ament, C.H. Wilson, and D.L. Burkhart contributed equally to this article.

Corresponding Author: Julian L. Griffin, University of Cambridge, 80 Tennis Court Road, Cambridge CB2 1GA, United Kingdom. Phone: 44-0-1223-42-6356; Fax: 44-0-1223-43-7515; E-mail: jules.griffin@mrc-hnr.cam.ac.uk

doi: 10.1158/0008-5472.CAN-15-3403

AACR

Overall, we established the lipid signatures for normal and tumor lung tissue in mice with increased MYC activity and endogenous levels of oncogenic KRAS. We found that normal tissue was predominantly characterized by pulmonary surfactant lipids, whereas tumor tissue had increased signaling precursor phospholipids, such as the phosphatidylinositols and arachidonate-containing phospholipids. We observed an increase in free arachidonic acid, which is released from membrane phospholipids by cytosolic phospholipase A2 (cPLA2), in tumors with high MYC activity and linked this to increased cPLA2 activity. Moreover, we report evidence at the metabolite and gene-expression level, linking MYC to increased synthesis of arachidonic acid-derived eicosanoids via the lipoxygenase (LOX) and COX pathways. Following MYC deactivation, specific metabolites and mRNAs associated with these pathways, and cPLA2 activity, decreased with time. By inhibiting the COX and 5-LOX pathways in high MYC mice, a reduction in tumor proliferation and increase in apoptosis was observed, highlighting these pathways as potential drug targets for lung cancer.

Materials and Methods

Tumor models

Lung tumors were generated by intranasal delivery of adeno-Cre (7×10^6) virus particles to either *Kras*^{tm4Tyj}(*LSL-Kras*^{G12D}) mice, which express oncogenic *Kras*^{G12D} upon Cre-mediated deletion, or *LSL-Kras*^{G12D}; *R26*$^{LSL\text{-}CAG\text{-}c\text{-}MycER/LSL\text{-}CAG\text{-}c\text{-}MycER}$ (*R26*$^{LSL\text{-}CMER}$) mice, which in addition to oncogenic KRAS express a high level of deregulated c-MYCER^{T2} [driven by a CAGGs (chicken β-actin/CMV) enhancer] from the *Rosa26* locus. The *Rosa26* model of c-MYCER^{T2} is regulated at two levels; expression of cre-recombinase is necessary to remove the stop element and addition of tamoxifen to the diet is necessary to activate the c-MYCER^{T2} protein, providing a means to activate or deactivate MYC (19). Detailed characterization of this novel mouse model will be described elsewhere (manuscript in preparation).

Ten adeno-Cre–injected *LSL-Kras*^{G12D};*R26*$^{LSL\text{-}CMER}$mice were fed a tamoxifen-containing diet for 4 weeks. Tamoxifen was removed from the diet for 24 hours ($n = 3$) or 72 hours ($n = 3$), to deactivate MYC (referred to as "MYC inactive") before culling. The remaining mice ($n = 4$, referred to as "MYC activated") were maintained on the tamoxifen-containing diet continuously. As a further control and to ensure the overall lipid content was not altered by the addition/removal of tamoxifen, *LSL-Kras*^{G12D} mice, where MYC expression was not controlled (referred to as "KRAS only"), were maintained either on a tamoxifen-containing ($n = 2$) or normal diet ($n = 2$). Lung samples were collected, snap-frozen with liquid nitrogen and stored at −80°C. Samples were embedded in Tissue-Tek OCT and 12-μm frozen sections on glass microscope slides were prepared using a cryostat. Adjacent sections were stained with hematoxylin and eosin (H&E). All animal procedures were approved by the UK Home Office and the University of Cambridge.

MALDI imaging MS

Matrix solutions of 10 mg/mL [2,5-dihydroxybenzoic acid (DHB; Sigma-Aldrich) or 2, 4, 6-trihydroxyacetophenone monohydrate (THAP; Sigma-Aldrich)] were administered to the tissue surface using a nebulized sprayer (Suncollect MALDI spotter, KR Analytical Ltd.). Imaging experiments were carried out using a MALDI LTQ Orbitrap XL (Thermo Fisher Scientific) at 50-μm step increments across the tissue. The chemical composition of the lipid head group determines whether it has a greater propensity to form positive or negative ions. To detect as many different lipid species as possible, spectra were acquired in positive (DHB) and negative (THAP) ion mode, from 250 to 1,000 *m/z* at 60,000 resolution. Mass accuracy in positive and negative ion mode was approximately 1 and 10 ppm, respectively. Lipid identity was performed by accurate mass using the Lipid Maps database (accessed December 2015; ref. 20). The predominant fatty acid composition of lipids was confirmed where possible by collision-induced dissociation (CID). Na^+ and K^+ lipid adducts commonly observed in positive ion mode using MALDI have a low yield of stable charged fragments. Therefore, to improve fragmentation efficiency in positive ion mode, the formation of lithium adducts more prone to fragmentation (21) was induced by a 5-second washing step in lithium nitrate (100 mmol/L) before deposition of matrix, and the corresponding lithiated ions subjected to fragmentation by CID.

LESA-MS

Lipids were extracted using LESA at multiple user-defined points (1 mm^2) across the tissue surface by dispensing 0.8 μL 1:2:4 chloroform: methanol: isopropanol with 10 mmol/L ammonium formate, and incubating for 2.5 seconds. Analytes extracted from the surface were infused using a Triversa Nanomate (Advion BioSciences), with capillary voltage 1.4 kV, 0.3 gas flow for 1 minute into an LTQ Orbitrap Elite (Thermo Fisher Scientific). Spectra were acquired in positive and negative mode, from 200 to 1,000 *m/z* at 60,000 resolution.

Data processing

Data from MALDI-MSI were converted to imzML format for processing (22). Using an in-house R script ions were retained above a threshold intensity and the *m/z* ratio of ions detected were summed across integral regions of 10 ppm to allow for alterations in *m/z* mass accuracy across the experiment ("binning"). Only features detected above a threshold proportion of pixels were retained. Ion intensities were normalized to the total ion count, before creating two-dimensional ion images. Clustering of pixels was performed using *k*-means clustering (23), to define tumor and normal tissue regions, and to establish the average spectra in each region from the cluster centers (Supplementary Fig. S1).

Data from LESA-MS were converted to mzML format for subsequent data processing, and features were picked using an in-house R script. Orthogonal projection to latent structures discriminant analysis (OPLS-DA) models (24) were constructed using SIMCA 14 (Umetrics), following normalization to the total ion count, and Pareto scaling (25). For univariate statistics, *P* values were determined using Student *t* tests ($\alpha = 0.05$) and are adjusted for multiple testing using the Benjamini–Hochberg procedure.

Eicosanoid assay

Ten microliters of butylated hydroxytoluene (0.2 mg/mL, Sigma-Aldrich), 40 μL of an internal standard mix (containing 100 nmol/L each of 12-HETE-*D*8, PGE_2-*D*4, and 8-iso-$PGF_{2\alpha}$-*D*4, Cayman Chemical Company), and 1 mL of methanol were added to approximately 100 mg of frozen tissue sample, which

was homogenized using a TissueLyser (Qiagen Ltd.) for 10 minutes at 30 Hz. Samples were centrifuged (17,000 × *g*, 5 minutes) and the supernatants dried down under nitrogen and reconstituted in 40 μL 1:1 (v/v) methanol: water. Samples were analyzed on a QTRAP 5500 (ABSciex UK Limited) coupled to an ACQUITY Ultra Performance Liquid Chromatography (UPLC) system (Waters Ltd.). The mobile phase gradient (0.5 mL/min) is detailed in Supplementary Table S1; mobile phase A was 0.1% acetic acid in water, mobile phase B was 0.1 % acetic acid in acetonitrile: methanol 80:20. Sample was injected (10 μL) into a Kinetex 2.6 μm XB-C18 100 Å column (100 × 2.1 mm, Phenomenex) at 30°C. The electrospray source was operated in negative ion mode (4.5 kV and 650°C). Mass transitions of 51 analytes and 3 isotopically labeled standards (Supplementary Table S2) were acquired in scheduled MRM mode. Peaks were integrated by the Quantitation Wizard within Analyst version 1.6 and normalized against wet tissue weight and to the intensity of the internal standards.

IHC

Staining was performed on 4-μm paraffin-embedded sections. Sections were deparaffinized, treated with citrate buffer for epitope retrieval, and endogenous peroxidases blocked in 3% H_2O_2. Immunohistochemical staining was performed using the Rabbit VECTASTAIN ELITE ABC horseradish peroxidase kit (Vector Laboratories) following the manufacturer's protocol. Primary antibodies were anti-Ki67 (Thermo Scientific; clone: SP6; 1:200), anti-caspase-3 antibody (Cell Signaling Technology; clone; 5A1E 1:2,000), anti–c-MYC antibody (Y69; Abcam; ab32072; 1:1,000), anti-phospholipase A2 (Abcam; ab58375: 1:1,000) and anti-phospholipase A2 (phospho Ser505; Abcam; ab53105; 1:200). Staining was imaged on a Zeiss Axio Imager using the Zeiss AxioVision 4.8 software. Quantification was performed by counting number of positive cells per tumor area for 5 images; the mean of 5 raw counts was calculated and represents one data point per graph.

Phospholipase A2 activity assay

Enzymatic activity was assessed using the Cytosolic Phospholipase A2 Assay Kit (Abcam; ab133909) following the manufacturer's instructions. Calcium-independent PLA2 activity was inhibited by the addition of bromoenol lactone, and secretory PLA2 isoforms removed using a membrane filter with the molecular weight cut-off value 30 kDa. Activity was normalized to total protein content.

Transcript quantification by qPCR

Total RNA was extracted and purified from homogenized frozen lung tissue (20 mg) using the RNeasy Mini Kit (Qiagen), following the manufacturer's protocol. Purified RNA concentration was quantified at 260 nm using a NanoDrop 100 (Thermo Fisher Scientific). Genomic DNA contamination was eliminated and complimentary DNA produced using the RT^2 First Strand Kit (Qiagen). Relative abundance of transcripts of interest was assessed by quantitative-PCR in RT^2 SYBR Green Mastermix (Qiagen) with a StepOnePlus detection system (Applied Biosciences). RT^2 primer assays for mouse *Rn18s* (endogenous control), *Pla2g4a* (*cPla2*), *Ptgs2* (*Cox2*), *Alox5*, *Alox15*, *Alox12*, *Tnf-α*, *Il1β* were obtained from Qiagen. Expression levels were normalized to endogenous controls using the $\Delta\Delta C_t$ method and fold changes reported were relative to the "KRAS-only" group (tamoxifen diet). Additional mouse lung samples were prepared such that 4 to 6 replicates were used per group. Statistical significance was determined using one-way ANOVA ($\alpha = 0.05$) and adjusted for multiple comparisons using the Holm–Sidak method.

In vivo inhibitor study

Eight adeno-Cre infected *LSL-Kras*^{G12D};*R26*$^{LSL\text{-}CMER}$ mice were fed a tamoxifen-containing diet as described above. Two weeks following the administration of tamoxifen diet, mice were treated with licofelone ($n = 4$) or vehicle ($n = 4$) once daily for 4 days, and culled 2 hours following the final treatment. Licofelone (Calbiochem; #435801), was freshly suspended in sunflower oil at a concentration of 20 mg/mL and given by oral gavage at a dose of 100 mg/kg.

Results

Tumors have distinct lipid signatures to normal tissue

First, we sought to characterize the lipid signature in KRAS-driven lung tumors with increased MYC activity, and compare this to the lipid profile of adjacent normal tissue using MALDI-MSI. To distinguish between normal and tumor tissue, pixels of each image were clustered according to their spectral similarity (Fig. 1A). This was validated by comparing with histologic features in adjacent H&E-stained sections (Fig. 1), and the average spectra of the tumor and normal tissue in both positive and negative mode compared (Fig. 1B and C). Using their accurate masses, and database searching (Supplementary Table S3) the majority of ions observed in positive ion mode were found to be sodiated (Na^+) and potassiated (K^+) adducts of phosphatidylcholines (PC) and their corresponding fragment ions (partial loss of head group, Δ *m/z* 59.074), whereas in negative ion mode spectra were predominantly characterized by deprotonated phosphatidylinisotols (PI), phosphatidylglycerols (PG), and free fatty acids (FFA). Characteristic product ion spectra were used to confirm lipid class and fatty acid composition (Supplementary Table S4).

Notable differences were observed in the lipid profiles of normal and tumor tissue (Figs. 1B and 2A). We found that the lipid profile of normal tissue was predominantly characterized by PC(32:0) (*m/z* 756.550 $[M+Na]^+$ and *m/z* 772.526 $[M+K]^+$; composed of fatty acids 16:0/16:0 according to fragmentation data; Supplementary Table S4) and PC(32:1) (*m/z* 754.535 $[M+Na]^+$ and *m/z* 770.510 $[M+K]^+$; 16:0/16:1). In contrast, tumor tissue contained a wider distribution of lipids, including PC(34:1) (*m/z* 782.568 $[M+Na]^+$ and *m/z* 798.542 $[M+K]^+$; 16:0/18:1) and PC(34:2) (*m/z* 780.552 $[M+Na]^+$ and *m/z* 796.526 $[M+K]^+$; 16:0/18:2). In particular, PC(36:4) (*m/z* 804.552 $[M+Na]^+$ and *m/z* 820.526 $[M+K]^+$; 16:0/20:4) had a significantly increased relative abundance in tumors compared with normal tissue. Ion images for the two most distinguishing ions, PC(32:0) $[M+Na]^+$ for normal tissue and PC(36:4) $[M+K]^+$ for tumors, were created highlighting their regiospecificity (Fig. 2B and C). Interestingly, differences were observed for the distribution of salt adducts, with a higher proportion of sodiated lipids present in normal tissue, and potassiated lipids in tumor regions (Fig. 2D–F).

Similarly, the lipid profiles in negative ion mode were examined (Fig. 1C; Supplementary Fig. S2). The most abundant species in both tissue types was PI(38:4) (*m/z* 885.539 $[M-H]^-$; 18:0/20:4; Supplementary Table S3), whereas the second most

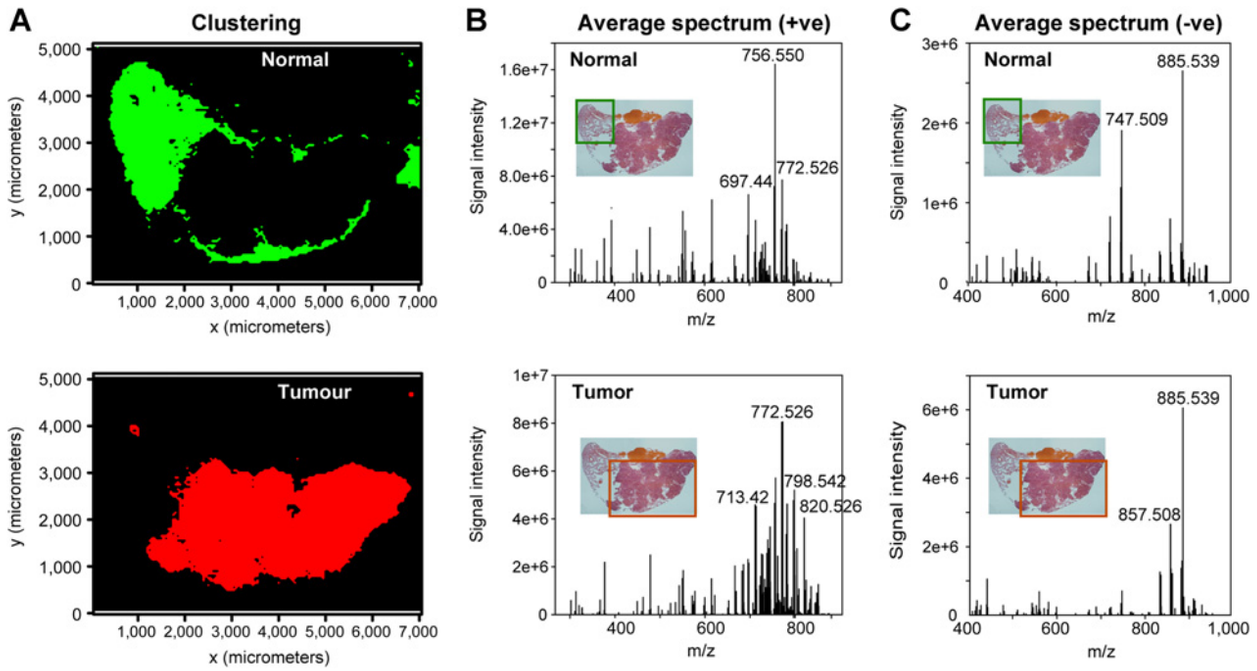

Figure 1.

Lipid signatures in normal and high MYC tumor tissue in lung. **A,** using MALDI-MSI and clustering, normal (green) and tumor (red) lung tissue were differentiated by their mass spectra. The average spectra in positive (**B**) and negative (**C**) ion modes for normal and tumor tissue clusters are shown. The inset shows an adjacent H&E-stained section of lung. Tumors are depicted by densely packed cells and stained dark pink, whereas normal tissue is thin and filled with voids. A blood vessel can be observed in the top center of the section (orange).

abundant species was PG(34:1) (*m/z* 747.509 $[M\text{-}H]^-$; 16:0/18:1) in normal tissue and PI(36:4) (*m/z* 857.508 $[M\text{-}H]^-$; 16:0/20:4) in tumor tissue (Fig. 1C; Supplementary Table S3). Overall tumor tissue had an increased relative abundance of PIs, whereas normal tissue had an increased relative PG content (Supplementary Fig. S2B and S2C). Free fatty acids revealed a relative increase in palmitic acid, FFA(16:0) $[M\text{-}H]^-$, in normal tissue and in arachidonic acid, FFA(20:4) $[M\text{-}H]^-$, in tumor tissue, in line with observations for the PCs (Supplementary Fig. S2A).

We complemented our results from MALDI-MSI with LESA-MS, which was carried out on different sections of the same samples (Supplementary Fig. S3). Lipids were extracted at multiple sites in both tumor and adjacent normal tissue and directly infused to the MS. Lipids identified in positive and negative ion mode were combined, and an OPLS-DA model built to identify which lipid species were important for classifying samples as either normal or tumor (Supplementary Fig. S3). Analysis supported the results from MALDI-MSI, and suggest that PC(32:0) $[M+H]^+$ was the most distinguishing ion for normal tissue, whereas free arachidonic acid and related lipids, including PC(36:4) $[M+H]^+$, were the most important lipid species differentiating tumor tissue.

Imaging MS distinguishes tumor models with different MYC activities

Having established the major differences in lipid profiles between normal and tumor tissue, we sought to identify the lipid profile differences attributable to high MYC activity. Removing tamoxifen from the diet results in rapid MYCER-fusion protein deactivation over the course of 24 hours (26). As a consequence of MYC deactivation, reduced tumor proliferation and apoptosis were observed (Supplementary Fig. S4A and S4B). Using MALDI-MSI, we therefore compared lung sections from *LSL-Kras*^{G12D};*R26*$^{LSL\text{-}CMER}$ mice with high MYC activity ("MYC activated") and those after 72 hours MYC deactivation ("MYC inactive"). As a control to ensure the overall lipid content was not altered by the addition of tamoxifen to the diet, we also examined lung tumors from *LSL-Kras*^{G12D} mice on a tamoxifen-containing diet, where MYC expression was low and unmodified ("KRAS only"; Supplementary Fig. S4C).

We examined the spatial distributions for PC(36:4) $[M+K]^+$ and PC(32:0) $[M+Na]^+$—the most distinguishing lipid species for tumor and normal tissue, respectively (Fig. 3A–C). A striking difference in the relative abundance of PC(36:4) was noted between the three tumor models (Fig. 3D). PC(36:4) accounts for a large proportion of the overall signal intensity in "MYC-activated" tumors (Fig. 3B). On the other hand, after deactivation of MYC the relative abundance of PC(36:4) in tumors was dramatically reduced (Fig. 3C). "KRAS-only" tumors had lower relative PC(36:4) content than "MYC activated," but higher than "MYC inactive," highlighting the effect that specific oncogenes or combinations thereof can have on the lipid profile. In-line with previous observations (27), PC(36:4) was also observed to localize prominently in the airway linings—this was more notable in the "MYC inactive" and "KRAS-only" samples.

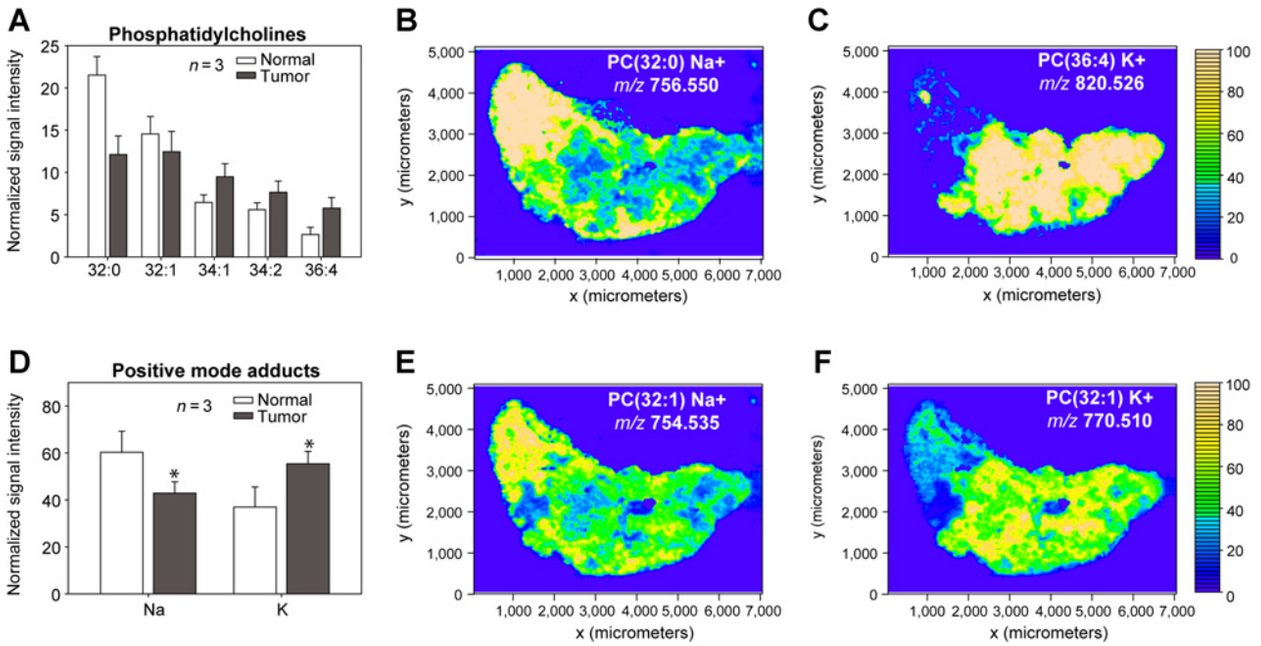

Figure 2.

Characterizing the lipidome in KRAS-driven lung tumors, with high MYC activity. Relative abundances of major phosphatidylcholines (PC) in tumor compared with normal lung tissue determined by MALDI-MSI. **A,** the intensities for multiple adducts were summed for each lipid species. **B** and **C,** two-dimensional ion images for PC(32:0) ([M+Na$^+$]; *m/z* 756.550; **B**) and PC(36:4) ([M+K$^+$]; *m/z* 829.526; **C**) show a predominantly normal or tumor tissue distribution, respectively. **D,** relative proportion of sodiated or potassiated PC adducts in tumor and normal tissue. **E** and **F,** MALDI-MSI images for sodiated (*m/z* 754.535; **E**) and potassiated (*m/z* 770.510; **F**) PC(32:1) show different spatial distributions. Data are mean (n = 3) ± SEM (*, P < 0.05).

MS suggests a role for arachidonic acid in MYC-dependent tumor models

We next focused on LESA-MS to further probe differences in the lipid profile for the three tumor types ("MYC activated," "MYC inactive," and "KRAS only"). Mass spectra were obtained in positive and negative ion modes. In positive ion mode, the most prominent lipids were protonated PCs (Fig. 4A). The lipid profiles for "MYC inactive" and "KRAS-only" tumor samples looked broadly similar, with a high relative content of PC (32:0) (*m/z* 734.569; [M+H]$^+$) and PC(32:1) (*m/z* 732.555; [M+H]$^+$). However, the lipid profile for "MYC-activated" tumor samples was strikingly different, with a notable relative increase in longer chain PCs, including PC(36:4) (*m/z* 782.569; [M+H]$^+$; Fig. 4A). In negative ion mode, a wider distribution of lipids was observed, including formate adducts of PCs, and deprotonated PIs, PGs, phosphatidylethanolamines (PE), plasmalogens, and free fatty acids (Fig. 4B). Of particular, note was a marked increase in the relative abundance of free arachidonic acid (*m/z* 303.234; [M-H]$^-$) in "MYC activated" tumors compared with "MYC inactive" and "KRAS-only" tumors (Fig. 4B).

Identified features in positive and negative mode were combined and used to construct an OPLS-DA (Fig. 4C) model. There was clear grouping of the three tumor classes (R^2 = 0.98, Q^2 = 0.91). Examination of the corresponding loadings plots (Fig. 4D) revealed that the most important lipid species for distinguishing "MYC activated" tumors was arachidonic acid, which was increased relative to the other two groups.

To further establish the changes in arachidonate, we examined the relative abundance of free arachidonic acid and related lipids, including its precursor linoleic acid [FFA(18:2)] and arachidonate-containing lipids PC(36:4) (16:0/20:4) and PC (38:4) (18:0/20:4). In all cases, a decrease over time was observed following deactivation of MYC: this was particularly notable for arachidonic acid itself. This can be attributed to the lower MYC level and not to diet, because lipid abundances in "KRAS-only" controls on normal and tamoxifen-containing diets were not significantly different (Fig. 4E).

Increased eicosanoids implicated in tumors with high MYC activity

Arachidonic acid is the major precursor for eicosanoids, important signaling molecules responsible for regulation of the inflammatory response, and implicated in facilitating cancer progression (28, 29). Because of their low abundance, eicosanoids and related lipid mediators are not easily detected by imaging techniques, and were therefore extracted from lung tissue and analyzed using liquid chromatography-tandem mass spectrometry (LC-MS/MS). On the basis of chromatographic retention times and characteristic fragmentation pathways (Supplementary Fig. S5; Supplementary Table S2), we detected 44 different eicosanoids and lipid mediators, 28 of which were derived from arachidonic acid. Identified species included 10 prostaglandins, 2 leukotrienes, 6 hydroxyeicosatetranoic acids (HETE), 4 epoxyeicosatrienoic acids (EET), 4 dihydroxyeicosatrienoic acids (DHETs), 3 hydroxyeicosapentaenoic acids (HEPE), 2 dihydroxyoctadecanoic acids (DiHOME), and

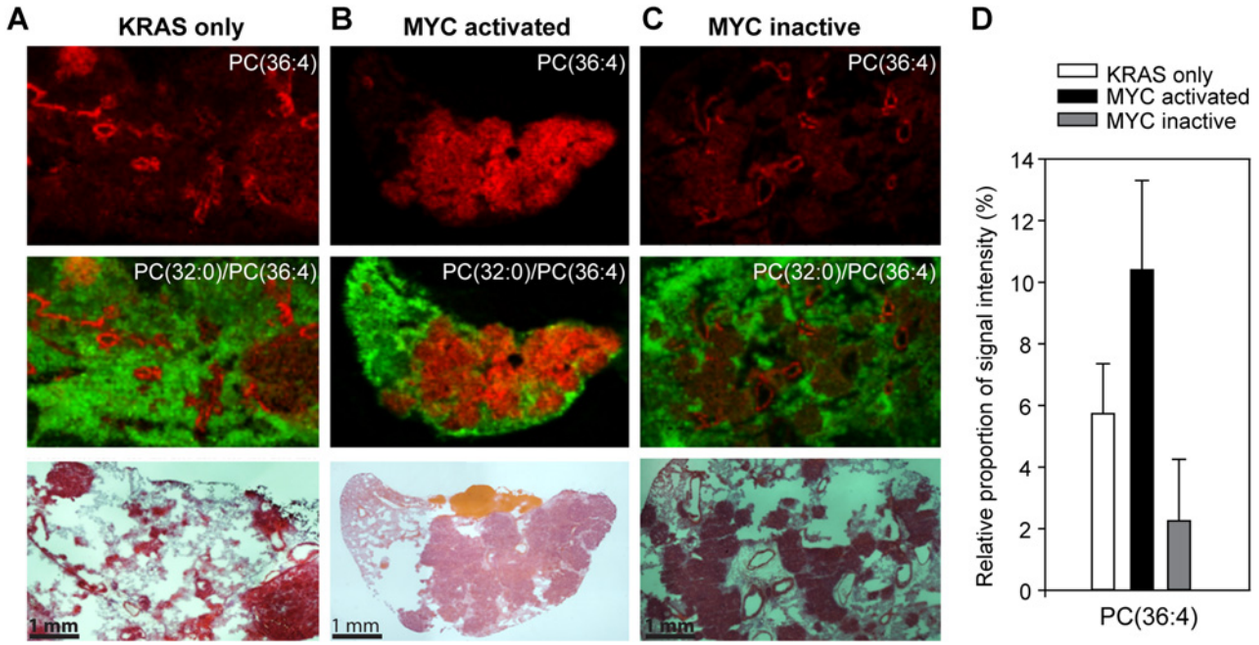

Figure 3.

MS imaging differentiates between levels of MYC activity. **A–C,** MALDI-MSI was carried out on lung tissue containing tumors driven by oncogenic KRAS only (**A**), with MYC activated (**B**), and with MYC deactivated for 72 hours (**C**). The spatial distributions of PC(36:4) [M+K^+] is shown in red (top) and overlaid with that of PC(32:0) [M+Na^+] in green (middle). Brighter intensity of color indicates higher ion abundance. Adjacent sections stained with H&E were used as a reference (bottom). **D,** the relative proportion of signal for PC(36:4) was compared for the three different tumors and found to be substantially higher in MYC-activated tumors. Data are mean (n = 2 or 3) ± SEM.

2 hydroxyoctadecadienoic acids (HODE). Interestingly, many of the identified species were found to be increased in "MYC-activated" samples, and the top 10 most increased eicosanoids were all arachidonic acid-derived (Supplementary Table S5). Using multivariate statistics (Supplementary Fig. S6A and S6B), we determined that the most important eicosanoids for distinguishing "MYC-activated" samples from the other groups were the HETEs, which were present at higher concentrations in "MYC-activated" samples (Fig. 4F). In addition to the HETEs, levels of prostaglandins (including PGE2 and PGF2α), thromboxanes (TxB2) and leukotrienes (LTB4), amongst others, were increased in "MYC-activated" lung tissue (Fig. 4F; Supplementary Table S5).

MYC linked to cPLA2 activity and COX/LOX expression

The observed increase in arachidonic acid-derived eicosanoids in "MYC-activated" tumors could arise from enhanced substrate availability through increased cPLA2 expression or activity, from increased expression of LOX/COX, or a combination of the above. To test this, we performed immunostaining on *LSL-Kras*^{G12D};*R26*$^{LSL\text{-}CMER}$tumors before and after MYC deactivation. We stained specifically for the active phosphorylated form (Fig. 5A), finding a higher number of positively-stained cells for the "MYC-activated" tumors, with a significant decrease over time following MYC deactivation (Fig. 5A and B). We then verified cPLA2 activity using an enzyme activity assay (Fig. 5C), which confirmed the significantly higher phospholipase activity in "MYC-activated" tissue. Interestingly, when examining the staining, we noticed that in many instances positively-stained cells were visibly undergoing cell division, suggesting a proliferative role for cPLA2 (Fig. 5D).

Next, we examined the gene expression in lung tissue from *LSL-Kras*^{G12D};*R26*$^{LSL\text{-}CMER}$mice, before and after MYC deactivation. We quantified transcripts for cPLA2 (*cPla2*), COX-2 (*Cox2*), 5-LOX (*Alox5*), 12/15-LOX (*Alox15*), and platelet-type 12-LOX (*Alox12*). As a reference group, we used lung tissue from *LSL-Kras*^{G12D} mice. No difference in *cPla2* mRNA levels was observed between whole lung tissue containing "KRAS-only" and "MYC-activated" tumors (Fig. 5E). However, upon MYC deactivation there was a significant increase in mRNA levels after 72 hours, which may be a compensatory effect to the overall reduction in cPLA2 activity. This suggests the changes observed in cPLA2 activity with MYC activation/deactivation are not governed at the transcriptional level. In contrast, transcript levels for *Cox2* and *Alox5* were significantly increased in "MYC activated" compared with "KRAS-only" lung tissue (Fig. 5E). Following MYC deactivation, these transcripts decreased with time, suggesting their amplification at the gene expression level is linked to MYC. Finally, we examined the gene expression for proinflammatory cytokines TNF-α and IL-1β, that may play a role in regulating cPLA2 and eicosanoid synthesis (30–33). We found a modest increase in *Tnf-α* with MYC activation, whereas *Il-1β* gene expression was closely correlated to MYC activity (Fig. 5F).

In vivo inhibition of COX/5-LOX pathways reduces proliferation in lung tumors

We have shown that COX-2 and 5-LOX transcripts and metabolites are linked to MYC activity in KRAS-driven adenocarcinoma. To confirm the importance and assess the feasibility of

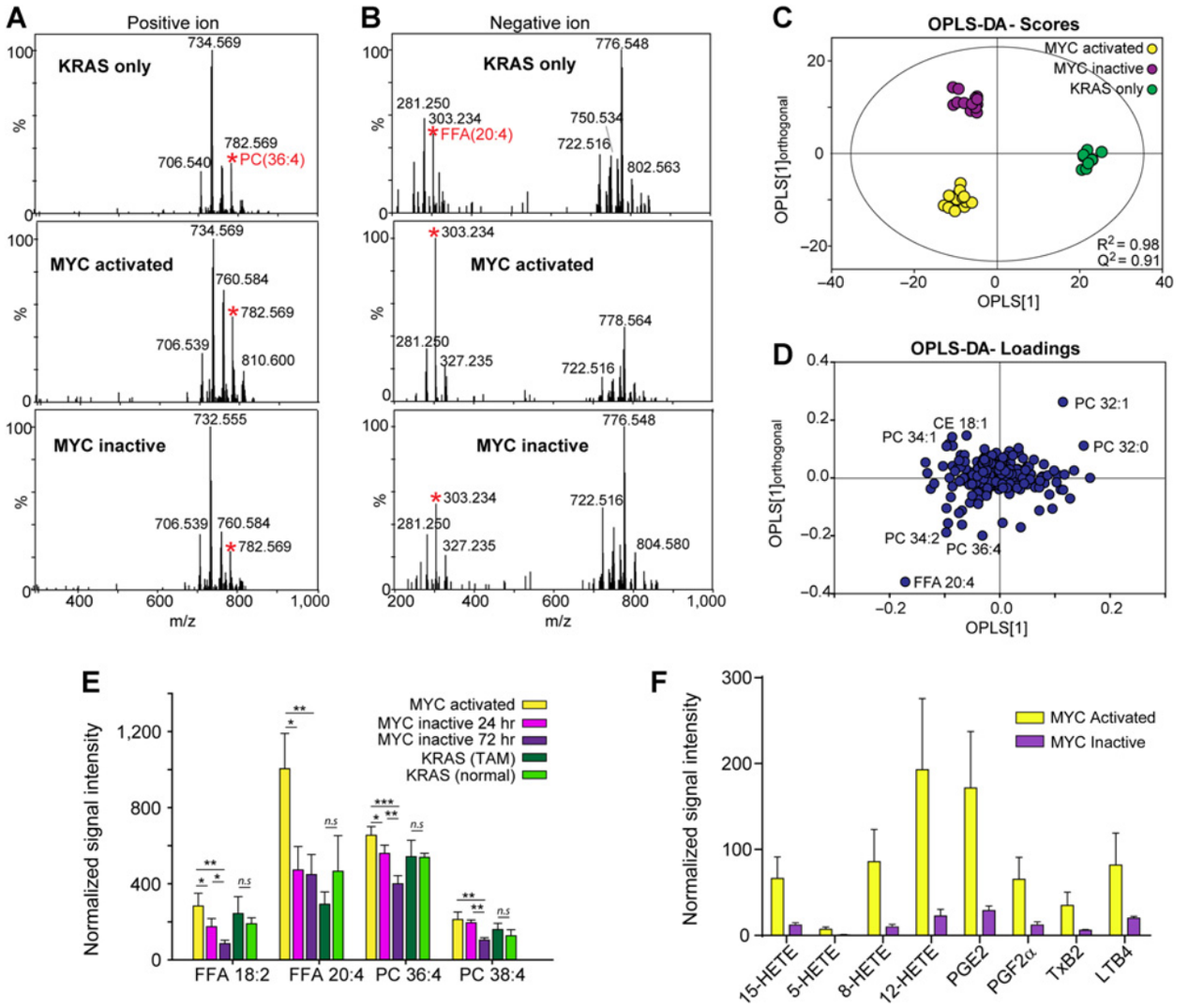

Figure 4.

Arachidonic acid-related lipids differentiate lung tumors with varying MYC activities. **A** and **B,** typical LESA mass spectra for lung tumors in positive (**A**) and negative (**B**) ion mode. Asterisks indicate PC(36:4) (*m/z* 782.569; $[M+H^+]$) and arachidonic acid (FFA(20:4), *m/z* 303.234; $[M\text{-}H^-]$). **C** and **D,** LESA-MS spectra at three sites across lung tumors ("MYC activated," $n = 4$; "MYC inactive," $n = 6$; "KRAS only," $n = 4$) were used to construct an OPLS-DA model (**C**) and related loadings (**D**) plot. A significant decrease over time was observed for arachidonic acid [FFA(20:4)] and related lipids following deactivation of MYC. **E,** MYC deactivation was achieved by the removal of tamoxifen from the diet; as an additional control, "KRAS-only" lung tumors from mice on a normal diet and a tamoxifen-containing diet were compared, with no significant (n.s) differences in lipid content noted. **F,** higher levels of eicosanoids, including HETEs, prostaglandins, and thromboxanes were measured by LC-MS/MS in "MYC-activated" compared with "MYC-inactive" samples. Data are mean ± SEM (*, $P < 0.05$; **, $P < 0.01$; ***, $P < 0.001$).

targeting these pathways for the treatment of such lung cancers, we designed an *in vivo* inhibitor study using the novel *LSL-Kras*^{G12D}; *R26*$^{LSL\text{-}CMER}$ mouse model, with MYC activated. Mice were infected with adeno-Cre and transferred to a tamoxifen-containing diet, as in the earlier experiments. Two weeks following the addition of tamoxifen, mice were treated with either vehicle or licofelone—a dual COX/5-LOX pathway inhibitor, which has shown promising chemopreventive efficacy in lung and colon cancers (34, 35). Remarkably, after only four doses we found substantially reduced tumor load when compared with vehicle-treated controls (Fig. 6A). To investigate this further, we performed staining for proliferation (Ki67; Fig. 6B and C) and apoptosis (cleaved caspase-3, Fig. 6D). We found increased apoptosis (although this did not reach significance) and significantly decreased proliferation (Fig. 6C) in tumors. Using mass spectrometry, we confirmed that the COX-2/5-LOX metabolites had been reduced, as anticipated (Fig. 6E).

Discussion

Here, we have probed the lipid profiles of mouse lung tumors with oncogenic KRAS and increased MYC activity, comparing

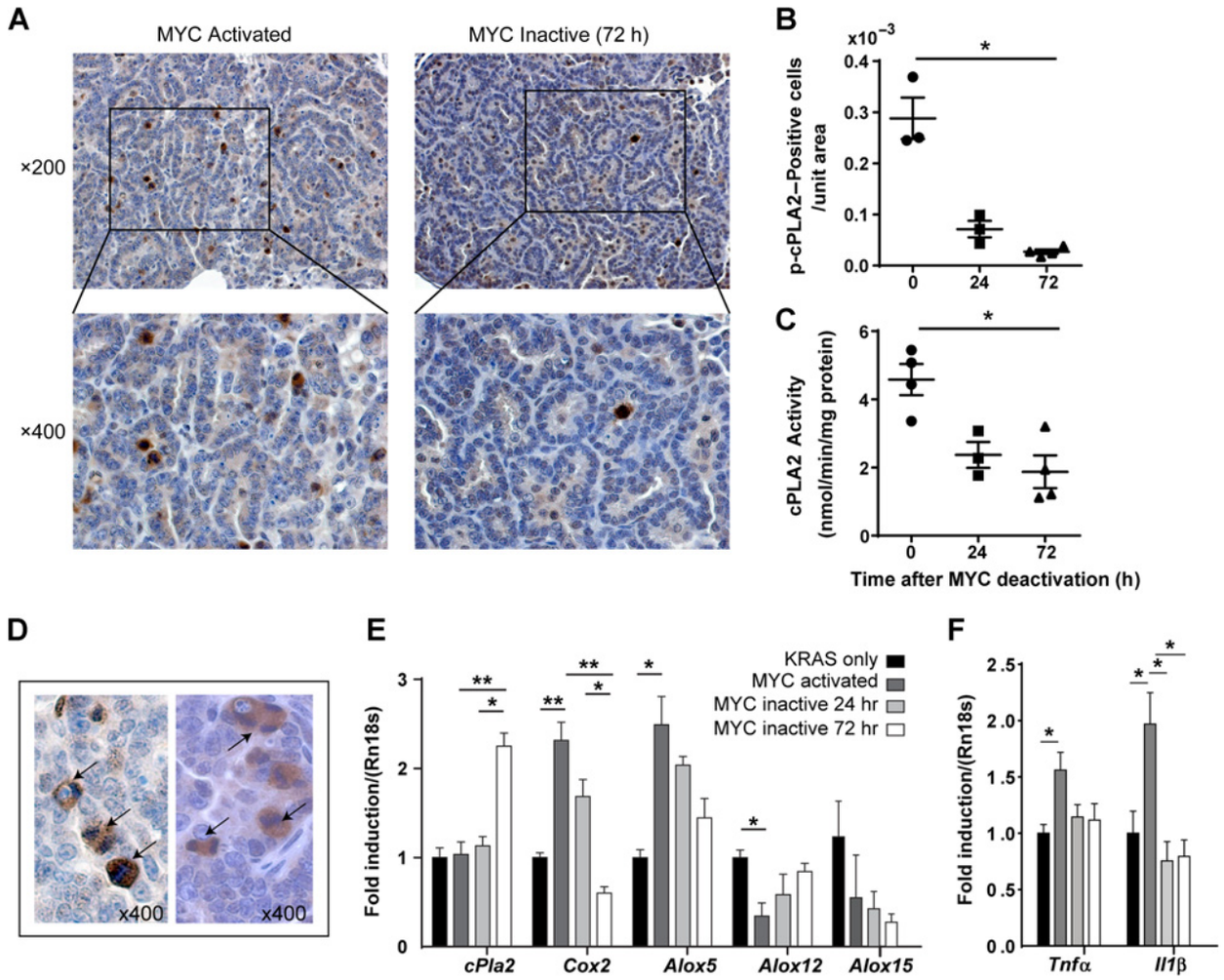

Figure 5.

Cytosolic phospholipase A2 activity linked to MYC. **A,** immunostaining of lung tumors for the active phosphorylated cPLA2 revealed a decrease in positively stained cells with MYC deactivation. **B,** quantification of staining revealed a significant decrease in phosphorylated cPLA2 levels with time after MYC deactivation. **C,** cPLA2 activity was determined using an enzyme assay and found to decrease with MYC deactivation. **D,** closer inspection of staining for phosphorylated (left) or total (right) cPLA2 revealed that many of the positively stained cells were visibly undergoing mitosis (black arrows). **E,** transcript quantification in lung revealed that only *Cox2* and *Alox5* mRNAs were increased in "MYC activated" compared with "KRAS-only" lung tissue. These levels decreased following MYC deactivation. **F,** similarly, *Tnf-α* and *Il-1β* mRNAs increased with MYC activation. Data are mean ± SEM (*, $P < 0.05$; **, $P < 0.01$).

normal and tumor tissue, and monitoring changes following the deactivation of MYC. The most intriguing discovery was a striking increase in arachidonic acid and arachidonate-containing phospholipids in "MYC activated" tumors compared with normal tissue. These levels dramatically decreased with time in tumors following MYC deactivation. Arachidonic acid is an omega-6 polyunsaturated fatty acid, and is liberated from membrane phospholipids by cPLA2 (28). The metabolism of arachidonic acid by COX, LOX, and cytochrome P450 generates eicosanoids, including prostaglandins, leukotrienes, and HETEs (Fig. 6F). Although the functional role of many eicosanoids remains unknown, a number act as potent mediators of inflammation, and have recently been implicated in cancers through effecting cell proliferation, survival, angiogenesis, migration, and invasion (36–38). In particular, arachidonic acid and its eicosanoid metabolites have been shown to activate peroxisome proliferator-activated receptors (PPAR), induce nuclear translocation of NF-κβ and to activate the PI3K signaling cascade (PI3K/AKT), a major driver for proliferation in cancer (33, 39).

In this study, we uncovered an increase in arachidonic acid–derived eicosanoids in cancerous lung tissue from "MYC activated" mice, notably metabolites of the COX and LOX pathways (Fig. 6F). We further found increased cPLA2 activity, which decreased with time following MYC deactivation, concomitant with decreased downstream metabolite levels. High cPLA2 staining was found in mitotic cells, suggesting a role for cPLA2 or its metabolites in proliferation. cPLA2 is activated by phosphorylation via the MAPK pathway, and effectors may include TNFα and IL1β, among many others (33, 40). Here, we found that gene expression for IL1β in particular was linked

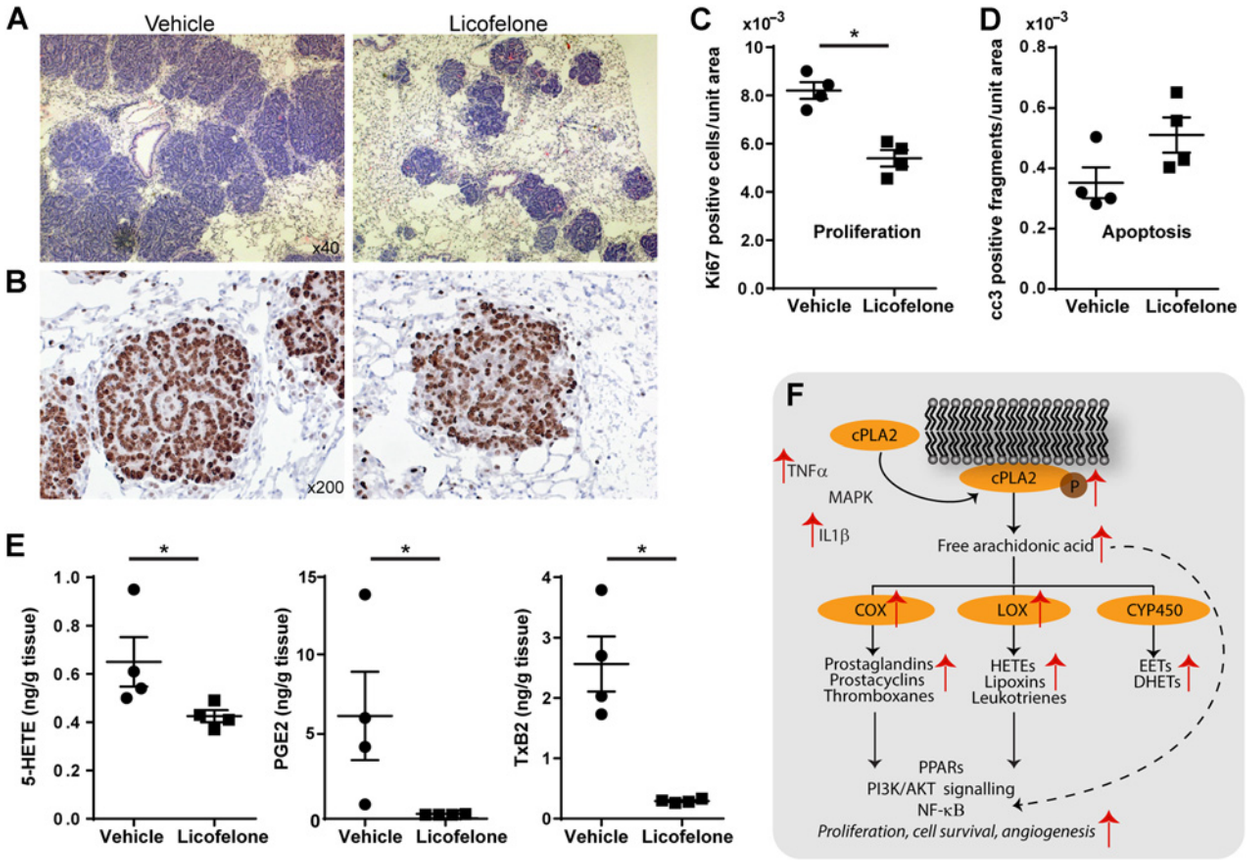

Figure 6.

In vivo inhibition of COX/5-LOX pathways. **A** and **B,** licofelone treatment in mice with KRAS-driven adenocarcinoma and high MYC resulted in reduced tumor load (H&E; magnification, ×40; **A**) and proliferation staining (Ki67; x200; **B**) compared with vehicle. **C** and **D,** quantification of proliferation (**C**) and apoptosis (**D**) by Ki67 and cleaved caspase-3 (cc3) immunostaining, respectively, was performed. **E,** LC-MS/MS confirmed reduction of 5-LOX and COX-2 metabolites. Data are mean ± SEM ($n = 4$); *, $P < 0.01$ (Mann–Whitney U test). **F,** cPLA2 is activated by phosphorylation through the MAPK pathway. Phosphorylated cPLA2 liberates arachidonic acid from intact phospholipids, which is metabolized by the COX, LOX, and cytochrome P450 pathways to form eicosanoids. Complex feedback mechanisms exist between LOX/COX, cPLA2 pathways, and proinflammatory cytokines such as TNFα and IL1β. Eicosanoids have a wide range of effects that can result in increased proliferation, cell survival and angiogenesis. Red arrows indicate a positive correlation to MYC activity level, as determined in this study.

to MYC activity. We additionally uncovered a link between upregulated COX-2 and 5-LOX gene expression and MYC activity. Interestingly, both genes contain an E-box sequence in their promoter region, so could be directly regulated by MYC abundance (41, 42). Alternatively, their response to MYC may be a result of complex interdependencies, occurring downstream of primary MYC targets. Inhibiting these two pathways *in vivo* resulted in marked reduction in tumor load and significantly decreased proliferation, highlighting their potential as targets for lung adenocarcinoma treatment, particularly with the involvement of MYC (43, 44).

Upregulation of lipid synthesis is a hallmark of cancers as a strategy to generate new cell membranes and signaling molecules, thus enabling the extensive proliferation of tumor cells (45). When comparing tumor and normal lung tissue, we observed a relative increase in PIs in tumors. PIs are precursors of the PI polyphosphates (PIP_n), an important class of signaling molecules involved in the PI3K signaling cascade. PIs are not considered to be rate-limiting for the formation of PIP_n, and their roles in many cancers are yet to be defined. However, specific PIs have been proposed as biomarkers for prostate cancer (46), and have been shown to be elevated in human lung tumors (47). One possibility here is that PI may provide an alternative source of arachidonic acid, because the most abundant PI identified was arachidonate-containing PI(38:4).

Although lipids serve as signaling precursors and structural components of the cell membrane, they also make up approximately 90% of pulmonary surfactant, which lines the alveolar surface of healthy lung. This fluid is responsible for reducing surface tension at the air-water interface, allowing efficient exchange of gases (48, 49). The lipid content of this surfactant is predominantly PC and PG, the most abundant of which are PC(32:0) (~50 %) and PC(32:1) (~10 %; refs. 27, 49). During our analysis, we found that PC(32:0), PC(32:1) and PGs were substantially increased in normal mouse lung tissue compared with tumor tissue. This may be as a result of the breakdown of the fine alveolar structure with tumor progression. An alternate explanation is the composition of surfactant in lung tumors

may be altered by catabolic phospholipase activity or acyl chain elongation (50).

Finally, differences were observed for the distribution of salt adducts, with a higher proportion of sodiated phospholipids present in normal tissue, and potassiated lipids in tumor regions. In healthy cells, there is typically higher intracellular K^+ whereas extracellular fluid such as lung surfactant contains a higher proportion of Na^+. This balance can be disrupted by the upregulation of Na^+/H^+ exchangers in cancerous cells with high aerobic glycolytic activity. Furthermore, dysregulation of potassium channels, Na^+/K^+ ATPase or Na^+/Ca^{2+} exchangers may also be important, particularly given the role of Ca^{2+} in cPLA2 activation (51, 52). All these could result in altered Na^+ permeability into the cell and/or export of K^+. An increased extracellular K^+ associated with tumors may account for the preference of K^+ adduct formation during ionization of phospholipids by MALDI-MSI, and offers unique insights into the tumor microenvironment.

Conclusion

Using a transgenic mouse model of KRAS-driven lung adenocarcinoma with reversible activation of MYC, we compared the lipid profiles of normal and tumor tissue, finding increased signaling-precursor lipids and eicosanoids, and decreased surfactant lipids in tumors. When MYC was deactivated, the tumor lipid signature markedly changed, with a large relative decrease in arachidonic acid and related lipids. This coincided with decreased cPLA2 activity and downstream metabolites, and decreased transcript levels for COX-2 and 5-LOX in lung tissue. We hypothesize that tumors with high MYC activity have increased levels of arachidonic acid as a consequence of increased cPLA2 activity. Free arachidonic acid serves as a substrate pool for upregulated eicosanoid synthesis, which can influence cancer progression in multiple ways. Dual inhibition of COX/5-LOX pathways *in vivo* resulted in reduced proliferation and a marked decrease in tumor load, and suggests these druggable pathways warrant further investigation as lung cancer therapies. MS imaging and associated surface analysis techniques have been shown here as powerful analytic tools, capable of obtaining detailed and spatially precise molecular signatures of tumor sub-environments, and paving the way for further studies in the exciting and rapidly developing field of lipidomics.

Disclosure of Potential Conflicts of Interest

No potential conflicts of interest were disclosed.

Authors' Contributions

Conception and design: Z. Hall, T. Ashmore, G.I. Evan, J.L. Griffin
Development of methodology: Z. Hall, A. Koulman, G.I. Evan, J.L. Griffin
Acquisition of data (provided animals, acquired and managed patients, provided facilities, etc.): Z. Hall, Z. Ament, C.H. Wilson, D.L. Burkhart, T. Ashmore, G.I. Evan
Analysis and interpretation of data (e.g., statistical analysis, biostatistics, computational analysis): Z. Hall, Z. Ament, T. Ashmore, J.L. Griffin
Writing, review, and/or revision of the manuscript: Z. Hall, Z. Ament, T. Ashmore, A. Koulman, T. Littlewood, J.L. Griffin
Administrative, technical, or material support (i.e., reporting or organizing data, constructing databases): C.H. Wilson
Study supervision: J.L. Griffin

Acknowledgments

We gratefully acknowledge Larissa Richardson and the Cambridge Advanced Imaging Centre for preparation of tissue sections for mass spectrometry experiments.

Grant Support

This research was funded by the Medical Research Council (Lipid Profiling and Signaling, MC UP A90 1006 & Lipid Dynamics and Regulation, MC PC 13030) and Cancer Research UK (program grant A12077).

The costs of publication of this article were defrayed in part by the payment of page charges. This article must therefore be hereby marked *advertisement* in accordance with 18 U.S.C. Section 1734 solely to indicate this fact.

Received December 13, 2015; revised May 10, 2016; accepted June 5, 2016; published OnlineFirst June 22, 2016.

References

1. The Cancer Genome Atlas Research Network. Comprehensive molecular profiling of lung adenocarcinoma. Nature 2014;511:543–50.
2. Robson SC, Ward L, Brown H, Turner H, Hunter E, Pelengaris S, et al. Deciphering c-MYC-regulated genes in two distinct tissues. BMC Genomics 2011;12:476.
3. Soucek L, Whitfield JR, Sodir NM, Masso-Valles D, Serrano E, Karnezis AN, et al. Inhibition of Myc family proteins eradicates KRas-driven lung cancer in mice. Genes Dev 2013;27:504–13.
4. Shachaf CM, Kopelman AM, Arvanitis C, Karlsson A, Beer S, Mandl S, et al. MYC inactivation uncovers pluripotent differentiation and tumour dormancy in hepatocellular cancer. Nature 2004;431:1112–7.
5. Baenke F, Peck B, Miess H, Schulze A. Hooked on fat: the role of lipid synthesis in cancer metabolism and tumour development. Dis Model Mech 2013;6:1353–63.
6. Louie SM, Roberts LS, Mulvihill MM, Luo K, Nomura DK. Cancer cells incorporate and remodel exogenous palmitate into structural and oncogenic signaling lipids. Biochim Biophys Acta 2013;1831:1566–72.
7. Hilvo M, Denkert C, Lehtinen L, Muller B, Brockmoller S, Seppanen-Laakso T, et al. Novel theranostic opportunities offered by characterization of altered membrane lipid metabolism in breast cancer progression. Cancer Res 2011;71:3236–45.
8. Brockmoller SF, Bucher E, Muller BM, Budczies J, Hilvo M, Griffin JL, et al. Integration of metabolomics and expression of glycerol-3-phosphate acyltransferase (GPAM) in breast cancer-link to patient survival, hormone receptor status, and metabolic profiling. J Proteome Res 2012;11:850–60.
9. Griffin JL, Lehtimäki KK, Valonen PK, Gröhn OHJ, Kettunen MI, Ylä-Herttuala S, et al. Assignment of 1H nuclear magnetic resonance visible polyunsaturated fatty acids in BT4C gliomas undergoing ganciclovir-thymidine kinase gene therapy-induced programmed cell death. Cancer Res 2003;63:3195–201.
10. Eberlin LS, Gabay M, Fan AC, Gouw AM, Tibshirani RJ, Felsher DW, et al. Alteration of the lipid profile in lymphomas induced by MYC overexpression. Proc Natl Acad Sci U S A 2014;111:10450–5.
11. Yuneva MO, Fan TW, Allen TD, Higashi RM, Ferraris DV, Tsukamoto T, et al. The metabolic profile of tumors depends on both the responsible genetic lesion and tissue type. Cell Metab 2012;15:157–70.
12. Angel PM, Caprioli RM. Matrix-assisted laser desorption ionization imaging mass spectrometry: *in situ* molecular mapping. Biochemistry 2013;52:3818–28.
13. Berry KA, Hankin JA, Barkley RM, Spraggins JM, Caprioli RM, Murphy RC. MALDI imaging of lipid biochemistry in tissues by mass spectrometry. Chem Rev 2011;111:6491–512.
14. Goto-Inoue N, Hayasaka T, Zaima N, Setou M. Imaging mass spectrometry for lipidomics. Biochim Biophys Acta 2011;1811:961–9.

15. Addie RD, Balluff B, Bovee JV, Morreau H, McDonnell LA. Current state and future challenges of mass spectrometry imaging for clinical research. Anal Chem 2015;87:6426–33.
16. Eikel D, Vavrek M, Smith S, Bason C, Yeh S, Korfmacher WA, et al. Liquid extraction surface analysis mass spectrometry (LESA-MS) as a novel profiling tool for drug distribution and metabolism analysis: the terfenadine example. Rapid Commun Mass Spectrom 2011;25:3587–96.
17. Griffiths RL, Dexter A, Creese AJ, Cooper HJ. Liquid extraction surface analysis field asymmetric waveform ion mobility spectrometry mass spectrometry for the analysis of dried blood spots. Analyst 2015; 140:6879–85.
18. Swales JG, Tucker JW, Spreadborough MJ, Iverson SL, Clench MR, Webborn PJ, et al. Mapping drug distribution in brain tissue using liquid extraction surface analysis mass spectrometry imaging. Anal Chem 2015;87:10146–52.
19. Murphy DJ, Junttila MR, Pouyet L, Karnezis A, Shchors K, Bui DA, et al. Distinct thresholds govern Myc's biological output *in vivo*. Cancer Cell 2008;14:447–57.
20. Sud M, Fahy E, Cotter D, Brown A, Dennis EA, Glass CK, et al. LMSD: LIPID MAPS structure database. Nucleic Acids Res 2007;35:D527–32.
21. Hsu F-F, Bohrer A, Turk J. Formation of lithiated adducts of glycerophosphocholine lipids facilitates their identification by electrospray ionization tandem mass spectrometry. J Am Soc Mass Spectrom 1998;9:516–26.
22. Rompp A, Schramm T, Hester A, Klinkert I, Both JP, Heeren RM, et al. imzML: imaging mass spectrometry markup language: a common data format for mass spectrometry imaging. Methods Mol Biol 2011;696: 205–24.
23. Hartigan JA, Wong MA. Algorithm AS 136: a K-Means Clustering Algorithm. J Royal Stat Soc C 1979;28:100–8.
24. Trygg J, Wold S. Orthogonal projections to latent structures (o-PLS). J Chemometrics 2002;16:119–28.
25. van den Berg RA, Hoefsloot HC, Westerhuis JA, Smilde AK, van der Werf MJ. Centering, scaling, and transformations: improving the biological information content of metabolomics data. BMC Genomics 2006;7:142.
26. Wilson CH, Gamper I, Perfetto A, Auw J, Littlewood TD, Evan GI. The kinetics of ER fusion protein activation *in vivo*. Oncogene 2014;33: 4877–80.
27. Berry KA, Li B, Reynolds SD, Barkley RM, Gijon MA, Hankin JA, et al. MALDI imaging MS of phospholipids in the mouse lung. J Lipid Res 2011;52:1551–60.
28. Dennis EA, Norris PC. Eicosanoid storm in infection and inflammation. Nat Rev Immunol 2015;15:511–23.
29. Astarita G, Kendall AC, Dennis EA, Nicolaou A. Targeted lipidomic strategies for oxygenated metabolites of polyunsaturated fatty acids. Biochim Biophys Acta 2015;1851:456–68.
30. Homaidan RF, Chakroun I, Dbaibo SG, El-Assaad W, El-Sabban EM. IL-1 activates two phospholipid signaling pathways in intestinal epithelial cells. Inflammation Res 2001;50:375–81.
31. Yang C-M, Lee I-T, Chi P-L, Cheng S-E, Hsiao L-D, Hsu C-K. TNF-α induces cytosolic phospholipase A2 expression via Jak2/PDGFR-dependent Elk-1/p300 activation in human lung epithelial cells. Am J Physiol 2014;306: L543–51.
32. McLeish KR, Knall C, Ward RA, Gerwins P, Coxon PY, Klein JB, et al. Activation of mitogen-activated protein kinase cascades during priming of human neutrophils by TNF-alpha and GM-CSF. J Leukocyte Biol 1998; 64:537–45.
33. Hyde CA, Missailidis S. Inhibition of arachidonic acid metabolism and its implication on cell proliferation and tumour-angiogenesis. Int Immunopharmacol 2009;9:701–15.
34. Sharma S, Lee J, Zhou J, Steele VE. Chemopreventive efficacy and mechanism of licofelone in a mouse lung tumor model via aspiration. Cancer Prev Res 2011;4:1233–42.
35. Mohammed A, Janakiram NB, Li Q, Choi CI, Zhang Y, Steele VE, et al. Chemoprevention of colon and small intestinal tumorigenesis in APC (Min/+) mice by licofelone, a novel dual 5-LOX/COX inhibitor: potential implications for human colon cancer prevention. Cancer Prev Res 2011;4:2015–26.
36. Wang D, Dubois RN. Eicosanoids and cancer. Nat Rev Cancer 2010;10: 181–93.
37. Greene ER, Huang S, Serhan CN, Panigrahy D. Regulation of inflammation in cancer by eicosanoids. Prostaglandins Other Lipid Mediat 2011;96:27–36.
38. Nie D, Honn KV. Eicosanoid regulation of angiogenesis in tumors. Semin Thromb Hemost 2004;30:119–25.
39. Hughes-Fulford M, Li CF, Boonyaratanakornkit J, Sayyah S. Arachidonic acid activates phosphatidylinositol 3-kinase signaling and induces gene expression in prostate cancer. Cancer Res 2006;66:1427–33.
40. Das S, Rafter JD, Kim KP, Gygi SP, Cho W. Mechanism of group IVA cytosolic phospholipase A(2) activation by phosphorylation. J Biol Chem 2003;278:41431–42.
41. Mestre JR, Rivadeneira DE, Mackrell PJ, Duff M, Stapleton PP, Mack-Strong V, et al. Overlapping CRE and E-box promoter elements can independently regulate COX-2 gene transcription in macrophages. FEBS Lett 2001; 496:147–51.
42. Zeller KI, Zhao X, Lee CWH, Chiu KP, Yao F, Yustein JT, et al. Global mapping of c-Myc binding sites and target gene networks in human B cells. Proc Natl Acad Sci U S A 2006;103:17834–9.
43. Sarveswaran S, Chakraborty D, Chitale D, Sears R, Ghosh J. Inhibition of 5-lipoxygenase selectively triggers disruption of c-Myc signaling in prostate cancer cells. J Biol Chem 2015;290:4994–5006.
44. Meyer AM, Dwyer-Nield LD, Hurteau GJ, Keith RL, O'Leary E, You M, et al. Decreased lung tumorigenesis in mice genetically deficient in cytosolic phospholipase A2. Carcinogenesis 2004;25:1517–24.
45. Santos CR, Schulze A. Lipid metabolism in cancer. FEBS J 2012;279: 2610–23.
46. Goto T, Terada N, Inoue T, Nakayama K, Okada Y, Yoshikawa T, et al. The expression profile of phosphatidylinositol in high spatial resolution imaging mass spectrometry as a potential biomarker for prostate cancer. PLoS ONE 2014;9:e90242.
47. Marien E, Meister M, Muley T, Fieuws S, Bordel S, Derua R, et al. Non-small cell lung cancer is characterized by dramatic changes in phospholipid profiles. Int J Cancer 2015;137:1539–48.
48. Akella A, Deshpande SB. Pulmonary surfactants and their role in pathophysiology of lung disorders. Indian J Exp Biol 2013;51:5–22.
49. Veldhuizen R, Nag K, Orgeig S, Possmayer F. The role of lipids in pulmonary surfactant. Biochim Biophys Acta 1998;1408:90–108.
50. Marien E, Meister M, Muley T, Gomez Del Pulgar T, Derua R, Spraggins JM, et al. Phospholipid profiling identifies acyl chain elongation as a ubiquitous trait and potential target for the treatment of lung squamous cell carcinoma. Oncotarget 2016;7:12582–97.
51. Haltiwanger S. Why electroporation is a useful technique for cancer treatments? In: SundararajanR, editor. Electroporation-based therapies for cancer: from basics to clinical applications.Cambridge, UK: Woodhead Publishing Series in Biomedicine; 2014. p. 103–25.
52. Amstalden van Hove ER, Blackwell TR, Klinkert I, Eijkel GB, Heeren RM, Glunde K. Multimodal mass spectrometric imaging of small molecules reveals distinct spatio-molecular signatures in differentially metastatic breast tumor models. Cancer Res 2010;70:9012–21.